Two-dimensional ion crystals in a hybrid optical cavity trap for quantum information processing

Zewen Sun,[1] Yi Hong Teoh,[1] Fereshteh Rajabi,[1,2] and Rajibul Islam[1]

[1]*Institute for Quantum Computing and Department of Physics and Astronomy, University of Waterloo, 200 University Avenue West, Waterloo, Ontario N2L 3G1, Canada*

[2]*Department of Physics and Astronomy, McMaster University, 1280 Main Street West, Hamilton, Ontario L8S 4L8, Canada*

(Received 1 September 2023; revised 8 February 2024; accepted 23 February 2024; published 22 March 2024)

We numerically investigate a hybrid trapping architecture for two-dimensional (2D) ion crystals using static electrode voltages and optical cavity fields for in-plane and out-of-plane confinements, respectively. By studying the stability of 2D crystals against 2D-3D structural phase transitions, we identify the necessary trapping parameters for ytterbium ions. Multiple equilibrium configurations for 2D crystals are possible, and we analyze their stability by estimating potential barriers between them. We find that scattering to antitrapping states limits the trapping lifetime, which is consistent with recent experiments employing other optical trapping architectures. These 2D ion crystals offer an excellent platform for quantum simulation of frustrated spin systems, benefiting from their 2D triangular lattice structure and phonon-mediated spin-spin interactions. Quantum information processing with tens of ions is feasible in this scheme with current technologies.

DOI: 10.1103/PhysRevA.109.032426

I. INTRODUCTION

Two-dimensional (2D) controlled many-body quantum systems, with their enriched phase diagrams, open up a new realm for physics study that is not readily accessible in one dimension, e.g., geometric magnetic frustration [1,2] and topological order [3,4]. Among all versatile quantum simulators, trapped-ion systems are an excellent platform to investigate quantum information processing (QIP) experiments [5,6]. Most conventional ion traps employ radio-frequency (rf) fields in addition to static (dc) potentials to create ion confinement. Typical geometrical constraints of rf-trap electrodes allow trapping of a chain of ions whose equilibrium positions are made to coincide with the "rf-null" line. This is to avoid the so-called micromotion-heating problem in which the driving rf fields cause unwanted heating of vibrational modes of ions that are used to mediate quantum entanglement. Despite recent efforts in developing rf traps with microfabricated electrodes for an ensemble of individual ions in a flexible geometry [7,8], creating a two-dimensional micromotion-free arrangement of ions remains a challenging technical task.

Two-dimensional ion systems for QIP have been proposed [9–12] and experimentally explored [7,8,13–22] with various technologies. For example, crystals of hundreds of ions in Penning traps, where the ion confinement is achieved with a static magnetic field and dc potentials, have been used to simulate two-dimensional Ising spin systems [13,16]. However, the ions rotate in the applied magnetic field of the Penning trap, creating additional challenges in optically addressing and measuring individual ion qubits. Another approach is to minimize the impact of micromotion by carefully choosing the geometries of laser beams that are used to address ions in conventional rf traps. Two-dimensional ion crystals have been studied in such systems for tens of ions [18,20,21], leading to experimental simulation of quantum magnetism [23–25]. Alternatively, the long-range Coulomb-mediated spin-spin interactions in an ion chain can be tailored to effectively create a two-dimensional spin system [26–28]. However, such synthetic systems often require fine-tuned static or dynamic controls over the Hamiltonian, which can be experimentally costly and error prone.

A way to obtain a rf-micromotion-free and nonrotating two-dimensional ion system is to employ optical trapping of ions, using the ac Stark shift from an optical beam. Indeed, optical tweezers [29,30] and optical lattices [31,32] have been used to trap ions in one dimension. However, the typical depth of the optical trapping potential is small compared to conventional rf and magnetic traps for experimentally feasible optical configurations. Further, the optical potential is dependent on atomic states, and hence, the lifetime of ions is limited by scattering from the optical beam into antitrapping or weakly trapped atomic states. The lifetime can be increased by reducing the rate of scattering by increasing the frequency separation ("detuning") between the light and relevant atomic transitions. For example, by changing the trapping beam from visible to near infrared, the lifetime of an optically trapped Ba^+ ion was experimentally demonstrated [33] to increase by a factor of 18 (from 166 ms to 3 s). However, increased detuning also necessitates higher optical intensity to create a deeper trapping potential suitable for a multi-ion system. A natural way to enhance the intensity of the optical field is to use a resonator cavity, which has been demonstrated as an excellent tool for trapping [34], modifying the trapping potential [35,36], and studying cavity quantum electrodynamics effects for ions [37,38]. In this paper, we study a hybrid trap architecture to trap 2D configuration of ions, in which the in-plane confinement is provided by the dc potential and the out-of-plane confinement is due to the optical standing wave in the cavity.

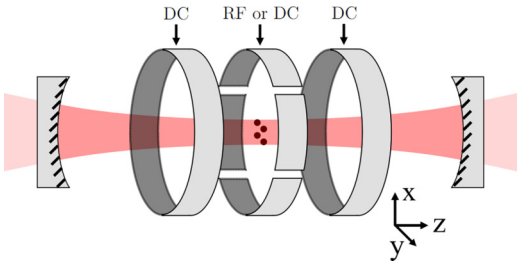

FIG. 1. Two-dimensional optical cavity trapping setup. Proposed 2D hybrid optical cavity trap setup (not to scale). Conventional trapping is provided by rf voltages on the central electrode and static (dc) voltages on the outer electrodes. Optical trapping along the z axis is provided by the ac Stark shift experienced by ions from the cavity-beam standing wave. The hybrid trapping consists of z trapping from the cavity beam and radial (x, y) trapping from dc voltages on the central electrode. Regarding the additional lasers for individual quantum control, they should propagate along the z axis to maximize optical resolution at individual ions. One can choose the cavity mirror coatings such that they reflect the trapping laser but transmit the control lasers.

This paper is structured as follows. In Sec. II, we discuss the hybrid trapping potential created in our architecture. We investigate the structural phase transition between 2D and three-dimensional (3D) configurations of ions as a function of trap anisotropy in Sec. III. We also find that the transverse size of the optical cavity mode with respect to the characteristic size of the ion crystal plays an important role in the structural phase transitions. Unlike in one dimension, two-dimensional ion crystals may have metastable equilibrium configurations [39,40]. In Sec. IV, we estimate the potential barrier between the stable and metastable configurations for up to $N = 9$ ions. We find that the potential barriers are higher than typical Doppler cooling temperatures. This may explain the stability of observed configurations in experiments with 2D ion crystals [20,21,40]. In Sec. V, we discuss the lifetime of multiple ions in the hybrid trap and identify the role of various heating mechanisms. The 2D arrangement of ions readily allows the creation of 2D spin models via the standard Mølmer-Sørensen scheme [5,41,42]. We discuss examples of spin-spin interactions between ions in 2D configurations suitable for simulations of geometrically frustrated magnetic models in Sec. VI. We also provide critical parameters (for Yb^+ ions) such as trap frequencies and the scattering rate for experimentally achievable laser parameters and optical cavities for a given target radial trap frequency.

II. OPTICAL 2D ION TRAPPING

The hybrid trapping architecture uses conventional trapping electrodes and a high-finesse optical cavity to trap 2D ion crystals, as schematically shown in Fig. 1. At first, the ions are trapped in a 2D configuration with conventional dc and rf voltages [20,21]. Then, the ions are transferred to the micromotion-free optical trap by adiabatically ramping up the laser intensity in the cavity and the dc voltages (on the central ring electrode in Fig. 1) while ramping down the rf potential and the dc voltages on the end electrodes. The inhomogeneous spatial distribution of the laser intensity from the standing wave created inside an optical cavity results in a position-dependent ac Stark shift, providing confinement in the z direction (i.e., out of plane for the 2D configuration). The trapping laser (with frequency ω_l) can be either "blue" ($\omega_l > \omega_a$) or "red" ($\omega_l < \omega_a$) detuned with respect to the relevant atomic transitions ω_a, determining the sign of the ac Stark shift and whether the ions are trapped in a node or antinode of the standing wave in the cavity.

In the hybrid optical trapping regime, we consider the total potential of the N-ion system U_{total}, consisting of three terms:

$$U^{\text{total}}\left(\{\mathbf{r}_i\}_{i=1}^N\right) = U^{\text{Coulomb}} + U^{\text{dc}} + U^{\text{opt}}, \tag{1}$$

where U^{Coulomb} is the Coulomb potential,

$$U^{\text{Coulomb}}\left(\{\mathbf{r}_i\}_{i=1}^N\right) = \sum_{i<j} \frac{e^2}{4\pi\varepsilon_0\|\mathbf{r}_i - \mathbf{r}_j\|}, \tag{2}$$

and U^{dc} is the potential from the dc circular electrode,

$$U^{\text{dc}}\left(\{\mathbf{r}_i\}_{i=1}^N\right) = \sum_i \frac{1}{2}m\left[\left(\omega_x^{\text{dc}}x_i\right)^2 + \left(\omega_y^{\text{dc}}y_i\right)^2 - \left(\omega_z^{\text{dc}}z_i\right)^2\right]. \tag{3}$$

Here, $\mathbf{r}_i$ is the position vector of ion i, m is the mass of the ion, ε_0 is the permittivity of free space, and ω_ξ^{dc} is the dc trap frequency, with $\xi \in \{x, y, z\}$. Here, we have assumed that the extent of the ion crystal in the radial direction is much smaller than the size of the dc electrodes, and hence, the anharmonicity in U^{dc} can be neglected. In addition, ω_z^{dc} should follow $(\omega_z^{\text{dc}})^2 = (\omega_x^{\text{dc}})^2 + (\omega_y^{\text{dc}})^2$ to satisfy Laplace's equation. The optical potential inside the cavity with a Gaussian trapping laser has the following form:

$$U^{\text{opt}}\left(\{\mathbf{r}_i\}_{i=1}^N\right) = U_{\text{depth}}^{\text{opt}} \sum_i \left(\frac{w_0}{w(z_i)}\right)^2 \exp\left(\frac{-2\left(x_i^2 + y_i^2\right)}{w^2(z_i)}\right) \times \sin^2\left(\frac{2\pi z_i}{\lambda}\right), \tag{4}$$

where w_0 is the beam waist of the Gaussian beam inside the cavity, $w(z_i)$ is the beam radius at position z_i, λ is the wavelength of the laser, and $U_{\text{depth}}^{\text{opt}}$ is the optical trap depth, defined as the absolute value of the maximum ac Stark shift, given by

$$U_{\text{depth}}^{\text{opt}} = \left|-\sum_a \frac{3\pi c^2}{2\omega_a^3}\left(\frac{\Gamma_a}{\omega_a - \omega_l} + \frac{\Gamma_a}{\omega_a + \omega_l}\right) I_{\max}\right|. \tag{5}$$

Here, c is the speed of light, Γ_a is the off-resonant scattering rate, ω_a is the atomic transition frequency between the ground state and excited state a, and $I_{\max}$ is the maximum intensity inside the cavity. Ions are trapped in the plane of $z = 0$ (see Fig. 1), and hence, the potential in the z direction [in Eq. (4)] can be assumed to be harmonic as well. We also assume that the center of the ion crystal is at the origin, $x = y = 0$. In this paper, we focus on $^{171}Yb^+$ ions, which are both a popular choice for QIP experiments and suitable for longer lifetimes in a far-red-detuned optical trap (with the wavelength of the optical trapping beam at 1064 nm).

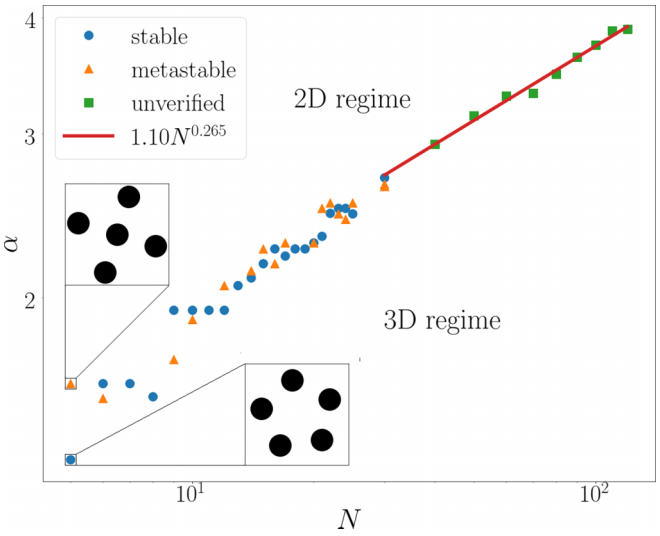

FIG. 2. The 2D-3D structural phase transition in ion crystals. Results are shown for a large cavity beam waist $w_0 = 100$ μm compared to the size (≈23 μm for $N = 100$) of the $^{171}Yb^+$ ion crystal, with $\omega_r^{dc}/2\pi = 0.5$ MHz. The determination of stable and metastable equilibrium positions is based on numerically calculated results (see text). For small $N \in [5,\ 30]$, we show the 2D-3D transition points with these stable (blue circles) and metastable (orange triangles) equilibrium positions. For large $N \in [40,\ 120]$, we do not verify whether the numerical equilibrium positions (green squares) are stable or metastable. The equilibrium points for $N \in [30,\ 120]$ are fitted with a power law to obtain an approximate scaling of the 2D-3D phase-transition points. Inset: Stable and metastable equilibrium configurations for $N = 5$.

III. STRUCTURAL PHASE TRANSITIONS

The anisotropy in trap frequencies determines whether a 2D ion crystal is stable against buckling into a 3D structure. We define the trap aspect ratio $\alpha \equiv \omega_z/\omega_r$, where $\omega_r \equiv \omega_x \approx \omega_y$, ω_z, and ω_r are the trap frequencies of the total potential at the origin. Here, the trap frequencies arise from both dc and optical trapping. The 2D-3D structural phase transition is analogous to the well-studied [43,44] "zigzag" phase transitions that arise in an ion chain. For α larger than the phase-transition point, α_{tr}, the ion crystal remains in the 2D phase. In addition to the trap aspect ratio, the 2D-3D structural phase transitions in the optical cavity trap potential also depend on the cavity beam waist w_0. Note that the 3D phase may be unstable if the trap depth along the z direction is not adequate.

Figure 2 shows the critical trap aspect ratio α_{tr} for various number of ions ($N = 8$ to $N = 120$) in the regime where the cavity waist w_0 is much larger than the size of the ion crystal r_{max}. We first calculate the equilibrium positions of the N-ion 2D crystal by numerically optimizing the total potential $U^{total}(\{\mathbf{r}_i\}_{i=1}^N)$ with respect to N-ion positions. In addition to the stable equilibrium configuration corresponding to the global potential minimum, there may exist metastable configurations corresponding to local minima as well [40]. However, we cannot verify whether a given equilibrium configuration is the true global minimum point of the potential. Instead, in calculating various possible equilibrium positions, we rerun our algorithm tens of times, with different initial guesses for the ion positions. If multiple equilibrium positions are obtained, we label the configuration with the minimum energy as "stable." Note that it is possible that our algorithm misses identifying other equilibrium configurations, one of which could be the true stable configuration. The 2D-3D structural phase-transition points will, in general, be different for stable and metastable configurations for the same N. We numerically find that the variations in α_{tr} are $\lesssim 5\%$ for up to $N \leqslant 25$, except for $N = 5$, 9, and 21, for which the variations are larger: 20%, 12%, and 7%, respectively.

The structural phase-transition point for a given equilibrium configuration can be numerically determined by monitoring the lowest out-of-plane normal-mode frequency ω^z_{lowest} as a function of ω_z while keeping the equilibrium positions of the 2D configuration fixed (i.e., keeping ω_r fixed). As ω_z decreases, ω^z_{lowest} decreases and eventually reaches zero. Any further decrease in α results in an imaginary ω^z_{lowest}, suggesting a breakdown in the normal-mode approximation around the chosen equilibrium position. The lowest normal-mode frequency $\omega^z_{lowest} = 0$ corresponds to the 2D-3D structural phase transition for the given 2D (stable or metastable) configuration. In Fig. 2, we show the structural phase-transition points for stable and metastable configurations for $N \leqslant 30$. However, numerically finding the true stable equilibrium configuration is challenging for a larger number of ions. Hence, for $N > 30$, we show the transition point for an equilibrium configuration without verifying whether that is a stable or metastable configuration.

The linearity of α_{tr} versus N in the log-log-scaled plot in Fig. 2, especially for large N ($\gtrsim$30), suggests that the transition points follow a power law, $\alpha_{tr} \approx 1.1N^{0.265}$. Our numerically obtained power-law exponent approximately agrees with the theoretical predictions in a harmonic potential for large N (up to $N = 500$), for which the exponents were calculated to be 0.25 [43] and 0.26 [44]. Considerable deviation from this power-law behavior is observed in both our numerics and the previous theoretical work [44] for small N.

When the cavity beam waist w_0 is smaller than or comparable to the size of the ion crystal r_{max}, ions at different locations experience substantially different local confinement. The 2D-3D structural phase-transition point is dependent on w_0 in this regime, as shown in Fig. 3. As w_0/r_{max} decreases, α scales up steeply, and a much higher out-of-plane trap frequency (at the origin) is required to maintain sufficiently strong out-of-plane confinement for outer ions for the 2D phase to be stable. For a given N, we find that α_{tr} does not show a strong dependence on the beam waist beyond a given w_0/r_{max}. For example, α_{tr} approaches its asymptotic value, corresponding to very large w_0/r_{max} for $N = 10$, at $w_0/r_{max} \approx 2.5$. A higher N corresponds to a smaller w_0/r_{max} at which the asymptotic limit is achieved. From a power-efficiency point of view, it is practically beneficial to choose a cavity beam waist close to this value to maximize the optical trap depth for the available optical power without being limited by the inhomogeneity in local optical confinement. Note that there may be additional considerations from the specific experimental protocol in choosing a cavity beam waist, such as the maximum allowable differential ac Stark shift difference between inner and outer ions, and the desired structure of the normal modes.

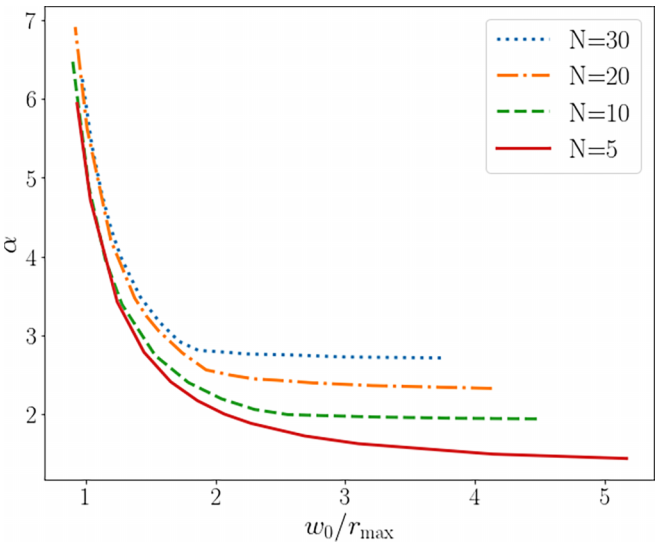

FIG. 3. Structural phase-transition points for ion crystals with different cavity beam waists. The 2D-3D structural phase-transition points for $^{171}Yb^{+}$ ions with $N = 5,\ 10,\ 20,\ 30$ (shown in different colors) versus beam waist w_0. The three curves are calculated using stable equilibrium positions. Ions are trapped in an optical cavity with $\omega_r^{dc}/2\pi = 0.5$ MHz.

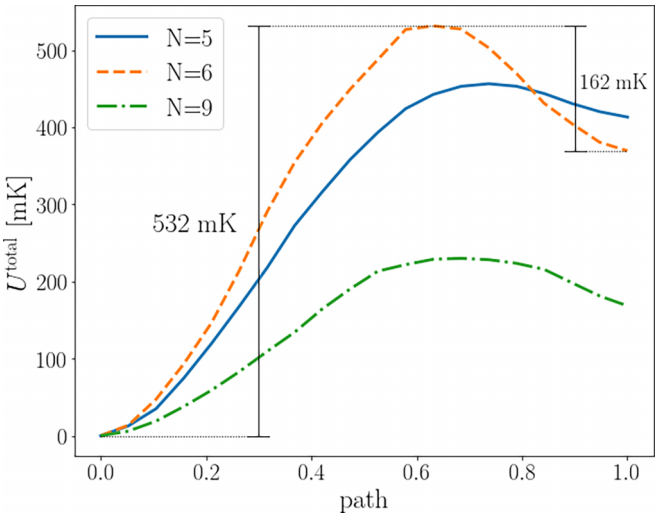

FIG. 4. Potential barrier between equilibrium configurations. The potential barriers are shown along numerically optimized paths between the two equilibrium configurations for various N (see Appendix B for the algorithm). On the horizontal axis, paths equal to 0 and 1 represent the stable and metastable equilibrium configurations, respectively. The potential energies of the stable equilibrium configurations with $N = 5$, 6, and 9 are set to zero for comparison purposes, but the three paths belong to different configuration spaces. The two potential barriers for $N = 6$ stable and metastable configurations (532 and 162 mK, respectively) are labeled. For $N = 7$ and 8, we find only one 2D equilibrium configuration.

With the study of structural phase transition combined with the trapping parameters illustrated in Sec. II, we find that it is feasible to trap ion crystals with several tens of ions in an optical cavity trap potential (see Appendix A).

IV. POTENTIAL BARRIER BETWEEN EQUILIBRIUM POSITIONS

Trapped ions experience various heating mechanisms, which can lead to a change in their equilibrium configuration, where multiple 2D equilibrium configurations exist. QIP experiments generally rely on optically addressing individual ions and exciting motional modes [41,42] that are specific to a given equilibrium configuration, and hence, a change in the ion configuration may be catastrophic. In this section, we numerically investigate the stability of 2D ion crystals by studying the potential barrier between equilibrium configurations, which quantifies the minimum kinetic energy required to transition between them.

Assuming that the out-of-plane trap frequency is strong enough that ions can move only in the $z = 0$ plane, each N-ion position is represented by a point in a $2N$-dimensional configuration space. When the N-ion system transitions from one equilibrium configuration to another, it traces a continuous path connecting the two equilibrium positions in the same space. We denote the maximum potential energy along the path as the peak potential for that path. Among infinitely many possible paths, we define the difference between the smallest peak potential and U^{total} of a given equilibrium configuration as its corresponding potential barrier.

To identify the path with the smallest peak potential and obtain upper bounds of potential barriers for a given N, we use the optimization algorithm discussed in detail in Appendix B. In Fig. 4, we show the results obtained using this optimization algorithm for 2D ion crystals with $N = 5$, 6, and 9. We find only one metastable equilibrium configuration for each N. For $N = 5$ and 9, the potential barriers corresponding to metastable equilibrium configurations (the right end of the plot) are around 40 to 60 mK, while the barriers for the stable configuration are 456 and 230 mK, respectively. For $N = 6$, the barrier for the metastable state is relatively higher (162 mK), while the barrier for the stable state (532 mK) is comparable to those for $N = 5$ and 9. We note that these values for the potential barriers are higher than the typical Doppler cooling temperatures, and hence, we do not expect to see fluctuations between these stable and metastable configurations unless we add extra energy into the system (e.g., during a nonadiabatic transfer from the conventional trap into the hybrid trap). The potential barrier corresponding to the metastable configuration can be comparable to the optical trap depth (can achieve at least ~100 mK in the optical cavity trap; see Table I), and hence, the stability of such configurations may be vulnerable to external perturbations. In that case, it will be desirable to obtain the stable 2D configuration in the conventional trap before transferring to the hybrid optical trap.

V. TRAPPING LIFETIME AND SCALABILITY

Compared to conventional potentials, optical potentials generally result in a significantly shorter ion-trapping lifetime [29,30,33]. Nevertheless, to be practically valuable, this platform requires optical trapping lifetimes that extend over at least the same timescale as quantum experiments involving

TABLE I. Optical trapping parameters for $^{171}Yb^{+}$. The ion configuration $[n_1, n_2, \dots]$ indicates that n_1 ions populate the "innermost ring," n_2 ions populate the next inner ring, and so forth. The trapping beam waist is determined from the ion crystal radius based on results from Fig. 3. For each N, the parameters are determined for the stable equilibrium position of the ion crystal. The ac Stark shift is the energy shift of the ground $^2S_{1/2}$ state. The differential shift is the difference between ac Stark shifts of two hyperfine states of the 6 $^2S_{1/2}$ manifold, $|F = 0, m_F = 0\rangle$ and $|F = 1, m_F = 0\rangle$, with a π-polarized laser, and the center refers to the center-of-equilibrium position of the ion crystal, whereas the edge is the position of the outermost ion. The minimum required optical power of the incident laser is calculated based on a cavity finesse of 3000. The scattering rate refers to the total off-resonant scattering rate of one ion under the minimum cavity intensity at the center of the ion crystal.

	Ion number N			
	5	10	20	30
Ion configuration	[5]	[2, 8]	[1, 7, 12]	[5, 10, 15]
Radial dc trap frequency ω_r^{dc} (MHz)	$2\pi \times 0.5$	$2\pi \times 0.5$	$2\pi \times 0.5$	$2\pi \times 0.5$
Laser wavelength λ (nm)	1064	1064	1064	1064
Minimum ion spacing (μm)	5.7	4.7	4.8	4.4
Ion crystal radius (μm)	4.8	7.8	10.9	13.4
Trapping beam waist w_0 (μm)	14.4	21.0	27.3	26.8
Minimum required ac Stark shift at center (MHz h)	287	361	475	600
[(mK)]	(13.8)	(17.3)	(22.8)	(28.8)
Differential ac Stark shift at center (kHz h)	15	19	26	32
Differential ac Stark shift at edge (kHz h)	7.7	9.0	12	12
Minimum required cavity intensity at center (W/m^2)	9.22×10^{11}	1.16×10^{12}	1.53×10^{12}	1.93×10^{12}
Cavity finesse $\mathcal{F}$	3000	3000	3000	3000
Minimum required laser power (W)	0.31	0.84	1.9	2.3
Off-resonant scattering rate of an ion at center Γ_{off} (s^{-1})	2.8	3.6	4.7	5.9

multiple ions (preferably 100 ms or more) [5]. The optical trapping lifetime is defined as the time it takes for the optical trapping probability p_{opt} to decrease to $1/e$, where p_{opt} is the probability of retaining all ions in the trap.

We find that scattering to antitrapping atomic states of the ion is the limiting factor for the optical trapping lifetime, consistent with the observations of prior optical trapping experiments [33]. For example, the metastable $^2D_{3/2}$ manifold of the $^{171}Yb^{+}$ ion experiences a positive ac Stark shift interacting with the 1064-nm Gaussian laser, and hence, the $^2D_{3/2}$ manifold is antitrapping. This manifold also has a relatively long atomic lifetime of 61.8 ms [45], during which ions can escape the trap. Since the trapping probability p_{opt} is defined for the N-ion system, the trapping probability for each ion at the end of the trapping lifetime should be $(1/e)^{1/N}$ such that $p_{\mathrm{opt}}(\tau) = 1/e$. If the scattering to metastable states is the only loss mechanism, we have

$$e^{-\Gamma_{\mathrm{meta}}\tau} = \left(\frac{1}{e}\right)^{1/N}, \tag{6}$$

$$\tau = \frac{1}{\Gamma_{\mathrm{meta}} N}, \tag{7}$$

where τ is the optical trapping lifetime and Γ_{meta} is the scattering rate to metastable states. For example, if the total off-resonant scattering rate for $^{171}Yb^{+}$ is $\Gamma_{\mathrm{off}} = 30$ s^{-1}, then $\Gamma_{\mathrm{meta}} = 0.15$ s^{-1} since the branching ratio between $^2P_{1/2} \rightarrow {}^2S_{1/2}$ and $^2P_{1/2} \rightarrow {}^2D_{3/2}$ is 200:1 [46]. For a 2D ion crystal with $N = 20$ $^{171}Yb^{+}$ ions, the scattering-rate-limited optical trapping lifetime is $\tau = 333$ ms. The loss due to scattering to metastable states becomes dominant for large N, providing an upper bound of $(\Gamma_{\mathrm{meta}} N)^{-1}$ for the optical trapping lifetime. If we apply a repumping laser actively transferring the population out of the metastable states, the optical trapping lifetime can be extended beyond this upper bound. For example, in Lambrecht *et al.* [33], the optical trapping lifetime of a single Ba^{+} ion was increased from 21 to 166 ms by applying repumping lasers, which is an increase of nearly 8 times. In the above analysis, we assume that each ion-loss event is independent of others and all ions have the same scattering rates.

In addition, collisions with background gas particles and the recoil effect from scattering can also heat up the system, although these effects are relatively minor (see Appendix C).

VI. VIBRATIONAL MODES AND SPIN-SPIN INTERACTIONS

Two-dimensional ion crystals exhibit a rich vibrational-mode structure. The highest-frequency mode along the out-of-plane direction is the center-of-mass (c.m.) mode, with the next-highest-frequency modes typically being the two tilt modes (see Fig. 5). Furthermore, Fig. 5 shows that the modes of the $N = 10$ 2D ion crystal have a composite structure composed of the typical modes in a one-dimensional (1D) chain, i.e., the c.m. mode, tilt mode, and a V-shaped mode. For example, the saddle$_{xy}$ mode is a composite mode of tilt$_x \times$ tilt$_y$. Additionally, we observe that the outer ions are the dominant participants in the higher modes and the inner ions are the dominant participant in the lower modes, with an exception being the c.m. mode, in which all ions participate equally. As there are more outer ions than inner ions, more energy is required to move the ensemble of outer ions compared to the ensemble of inner ions.

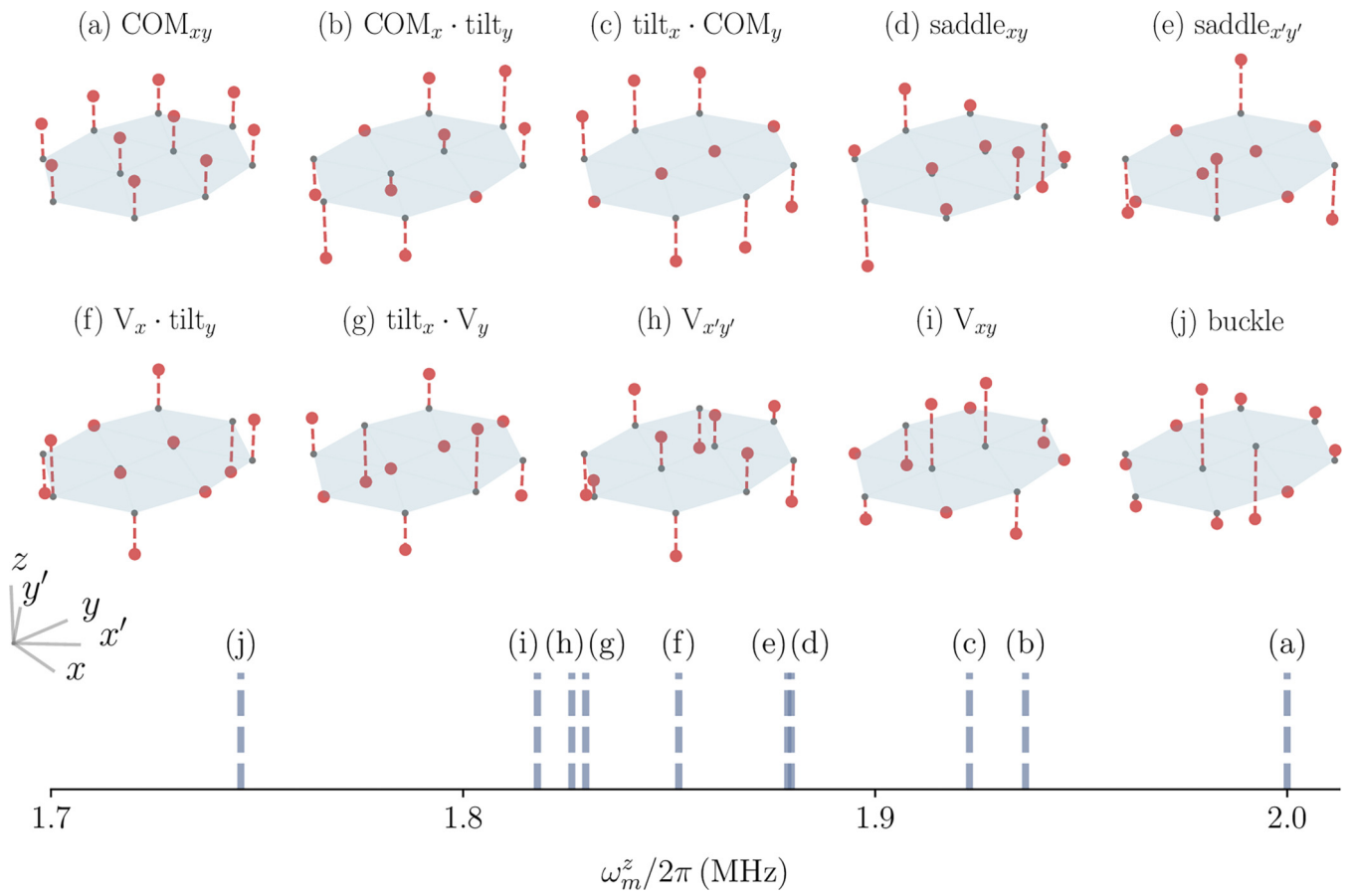

FIG. 5. Out-of-plane (z) vibrational modes of an $N = 10$ 2D ion crystal. The trap strengths are $\omega_r/2\pi \approx 0.5$ MHz and $\omega_z/2\pi = 2$ MHz for these numerical calculations. The mode labels are described in the text. To avoid degeneracies (see text) arising from rotational symmetry in the total potential U^{total}, we have introduced a 10 % anisotropy in the trap frequencies along the x versus y directions.

The equilibrium configuration of an ion crystal violates the underlying symmetry of a trap that is isotropic along the x and y directions (this is an example of spontaneous symmetry breaking). However, we find that multiple modes, e.g., the tilt modes, are still approximately degenerate for an isotropic trap. By introducing slight anisotropy (∼8%), the degeneracy in the tilt modes can be broken by approximately 0.5%; however, a greater anisotropy ($\gtrsim$20%) is needed to break the degeneracy of the saddle modes by a similar amount.

In the above calculations, we assumed that the cavity beam waist is much larger than the characteristic size of the ion crystal. For smaller cavity beam waists, there will be inhomogeneous trapping of the inner and outer ions, stronger on the inner ions and weaker on the outer ions. Consequently, the frequency and shape of the modes will change [47]. For example, the c.m. mode (with equal amplitude on all ions) will not be an exact eigenmode for a finite cavity beam waist. However, it is still an approximate mode. As an example, for $w_0 = 21$ μm and $r_{\text{max}} \approx 7.8$ μm (from Appendix A), the relative amplitudes of the weakest and strongest participating ions are approximately 0.56. Increasing the cavity beam waist will reduce the imbalance between the amplitudes of the participating ions in the c.m. mode [47].

As mentioned in Sec. III, the lowest-frequency mode plays an important role when characterizing the 2D-3D phase transition. Analogous to the zigzag phase in a 1D-2D phase transition, the 3D configuration resembles the eigenvector of the lowest-frequency mode; i.e., the middle ions buckle out of the 2D plane past the phase-transition point.

The rich vibrational-mode structure can be used to generate interesting spin-spin interaction profiles for the simulation of quantum spin models [5,6]. By applying suitable spin-dependent forces (SDFs) generated from laser beams, spin-spin interactions can be engineered with controls (in principle, arbitrary) over the strength, range, and sign of the interaction profile. Spin models such as the long-range Ising and XY models have been studied experimentally in a 1D chain in conventional rf traps [26,27,48,49] and also in 2D rotating crystals in Penning traps. Extending these protocol to 2D nonrotating crystals in our hybrid trap will enable access to more complex quantum simulations of spin models, such as 2D frustrated Hamiltonians.

In the commonly used Mølmer-Sørensen scheme [41,42], the effective Hamiltonian $\hat{H}$ of the trapped-ion system, when driven by multiple SDFs, is

$$\hat{H} = \sum_{i<j} J_{ij} \hat{\sigma}_i^{(x)} \hat{\sigma}_j^{(x)}, \tag{8}$$

where

$$J_{ij} = E_{\text{recoil}} \sum_n \Omega_{in} \Omega_{jn} \sum_m \frac{b_{im} b_{jm}}{\mu_n^2 - \omega_m^2}. \tag{9}$$

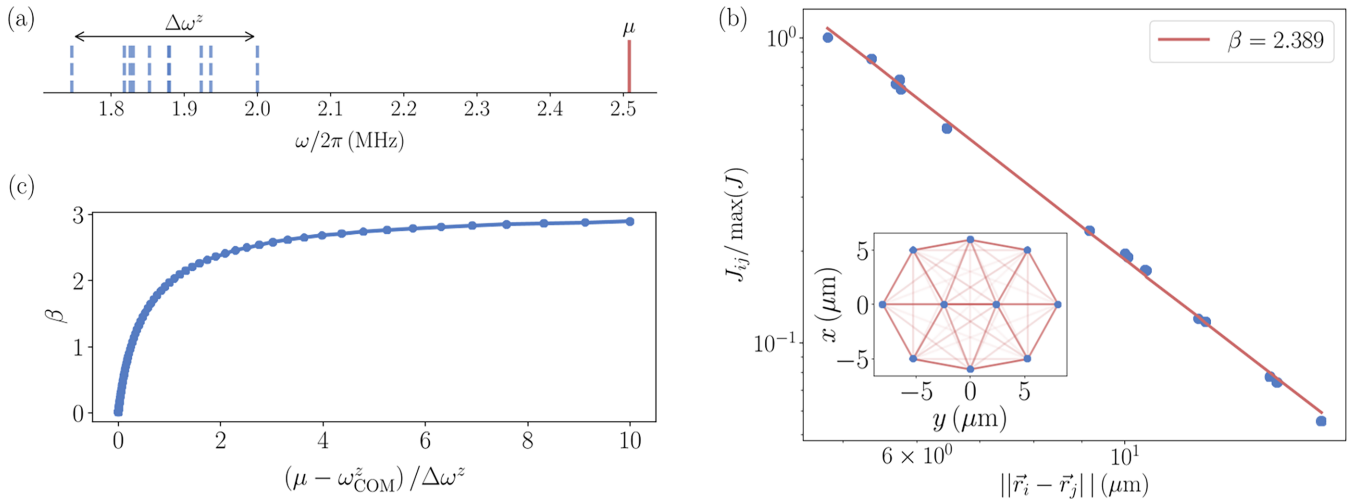

FIG. 6. Frustrated spin-spin interactions for $N = 10$ ions. (a) Out-of-plane (z) mode frequencies ω^z_m (blue dashed lines) alongside the SDF frequency μ (red solid line). (b) Spin-spin interactions J_{ij} [calculated from Eq. (9)] follow a spatial power-law decay with exponent β [Eq. (10)]. Inset: The resulting interaction graph. All the interactions are antiferromagnetic for this μ. The strongest interactions form a triangular lattice, creating a frustrated spin system. (c) Variation in β versus the SDF frequency.

Here, J_{ij} is the spin-spin interaction strength between ions i and j, $E_{\rm recoil}$ is the characteristic recoil energy from the laser field driving the SDFs, μ_n is the nth SDF frequency, ω_m is the mth normal-mode frequency, and Ω_{in} is the Rabi frequency of ion i for the nth SDF.

Like a chain of ions, a power-law interaction profile can be generated from a single SDF [5]. The form of the interaction is

$$J_{ij} \propto \frac{1}{\|\mathbf{r}_i - \mathbf{r}_j\|^\beta}, \tag{10}$$

where β is the power-law exponent. Figure 6 shows that the exponent β can be tuned between 0 and 3 for a 2D configuration when the SDF frequency is varied. A power-law-like interaction in the 2D configuration, in comparison with a 1D chain, exhibits magnetic frustration naturally due to the additional spatial degree of freedom and the configuration of the ions (shown in Fig. 6) resembling a triangular lattice.

Other lattice structures can be obtained via optical engineering of the Raman beams, similar to the case of 1D ion chains [26,27]. Alternatively, the triangular lattice can be further mapped to a square, kagome, or other lattice structure by augmenting the analog simulation with digital gates [28].

VII. CONCLUSION

To summarize, our study demonstrates the potential of utilizing an optical cavity to trap 2D ion crystals, offering enhanced trap depth and an extended lifetime compared to existing tweezer-based optical ion-trapping experiments. We estimate that the off-resonant scattering to antitrapping states from the cavity beam, rather than heating due to photon recoil and collisions, is the limiting factor for trapping lifetime, particularly for large N. To increase the optical trapping lifetime, one can either reduce the total off-resonant scattering rate or apply a repumping laser. An alternative approach could be to use ion species with a smaller atomic number, which do not have any metastable states between the lowest atomic S and P manifolds. However, there may be additional challenges when using such ions, such as a reduced ac Stark shift at the same optical intensity.

In addition, ions may be lost during the transferring process between conventional and optical trapping regimes if the transfer is not adiabatic enough to provide the ions with energy to overcome the optical trap depth. We may also want to minimize any motional excitation to avoid the necessity to cool the ions in the optical trap, as cooling protocols may populate antitrapping states. Due to the shallow optical trap depth, detection of quantum states involving ion fluorescence is likely not feasible without losing the ion from the trap. Thus, transferring the ions back into the conventional trap is preferable.

For QIP experiments with this system, the quantum coherence will be destroyed by all off-resonant scattering events, including those that do not lead to ion loss from the trap. Therefore, coherence time of the full system is typically much shorter than the optical trapping lifetime. The scattering rate-limited coherence time is proportional to $1/(\Gamma_{\rm off}N)$, where $\Gamma_{\rm off}$ is the total off-resonant scattering rate. Reducing the scattering rate $\Gamma_{\rm off}$ is the only way to overcome this fundamental limitation, leading to our choice of a 1064-nm laser for this proposal. Alternatively, blue-detuned lasers for trapping [50,51], where ions are trapped at the intensity minimum, can be investigated [52] to reduce scattering rates that limit the coherence time and trapping lifetime. However, as most ion species have relevant transitions in the ultraviolet regime, it may be challenging to create a deep optical potential with blue-detuned lasers. The suitability of red- vs blue-detuned trapping will also depend on the atomic structure of the species. For example, Ba^+ and Yb^+ ions have very different branching ratios into metastable D states, such that under the same $\Gamma_{\rm off}$, $\Gamma_{\rm meta}$ for Yb^+ is much lower than that for Ba^+. We think that the low $\Gamma_{\rm meta}$ makes Yb^+ a better candidate

compared to Ba^+ for red-detuned optical traps, but Ba^+ could be a potential candidate for blue-detuned optical traps.

ACKNOWLEDGMENTS

We acknowledge financial support from the Canada First Research Excellence Fund (CFREF), the Natural Sciences and Engineering Research Council of Canada (NSERC) Discovery program (RGPIN-2018-05250), University of Waterloo, and Innovation, Science and Economic Development Canada (ISED).

APPENDIX A: TWO-DIMENSIONAL OPTICAL TRAPPING PARAMETERS

Table I lists the minimum required trapping parameters for 2D ion crystals with different N to maintain the 2D regime. Radial dc trap frequency determines the 2D ion crystal size and ion spacing, which is chosen such that the ions can be optically addressed for QIP experiments with low cross talk between them [53].

Since the ac Stark shift and off-resonant scattering rate are proportional to intensity, the listed parameters help to reveal the proportionality constants. The listed minimum required laser power is less than the damage threshold for cavity mirror coatings, and is practically achievable. Hence, the optical trap depth can be significantly improved beyond the listed minimum ac Stark shift.

APPENDIX B: OPTIMIZATION ALGORITHM FOR POTENTIAL BARRIER

In Sec. IV, potential barriers between stable and metastable equilibrium positions of the 2D ion crystal were studied and presented. The following optimization algorithm is used to identify the path with the smallest peak potential. This algorithm has the following steps:

(1) For a 2D N-ion crystal, the stable equilibrium position is set to be the initial point $\mathbf{x}_i$ for $i = 0$, and a metastable equilibrium position is set to be the final point $\mathbf{x}_f$. The points are defined in the $2N$-dimensional configuration space.

(2) Define a neighborhood space of $\mathbf{x}_i$ with linear size ε, as shown in Fig. 7, which contains a set of N-ion positions that are relatively close to the initial point.

(3) Select all points in the neighborhood space that are closer to the final equilibrium position by a distance d or larger, which is the gray region in Fig. 7. Since the size of the neighborhood space scales up exponentially with respect to N, numerically selecting all the points is not feasible. Instead, $n_r = 1000$ randomly sampled points in the gray region are selected. We choose $d \approx \|\mathbf{x}_0 - \mathbf{x}_f\|/20$ and neighborhood-space linear size $\varepsilon = 2.5d$.

(4) Calculate the potential energy of all the selected points in the neighborhood space.

(5) Assign each selected point a transition probability according to the Boltzmann probability distribution

$$p_j = \text{normalize}\left[e^{-(E_j - E_i)/k_B T_\text{p}}\right], \tag{B1}$$

where E_i is the potential energy of the initial point, E_j is that for the selected point, and k_B is the Boltzmann constant. T_p is a hyperparameter with units of temperature, which determines the volume of the trajectory space under consideration. We empirically choose $T_\text{p} = 1$ mK, which is comparable to the temperature of a Doppler-cooled ion.

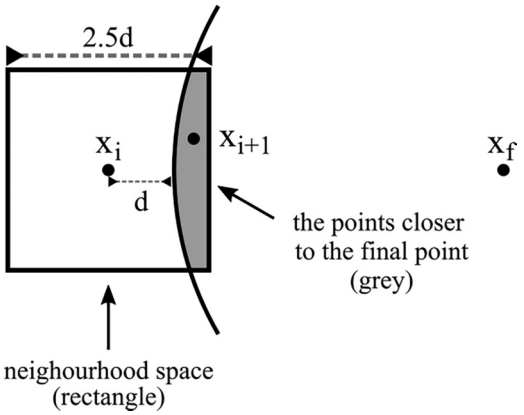

FIG. 7. Schematic diagram of one iteration in the optimization algorithm.

(6) Take a sample (denoted as x_{i+1}) from the selected points according to the transition probability p_j.

The sampled x_{i+1} in step 6 will replace the initial point x_i in step 2, and by repeating steps 2–6 until the distance between the sampled point and the final point is smaller than d, a path connecting the initial and final equilibrium positions can be obtained using this algorithm. This algorithm biases the trajectories towards smaller potential peaks. We calculate 10 paths with this approach and take the smallest potential peak to find an upper bound of the potential barrier. Figure 4 plots the trajectory with the smallest potential peak for a given N.

APPENDIX C: HEATING EFFECTS

The theoretical estimation of the optical trapping lifetime is based on the analysis of the ion scattering rate and different heating mechanisms. In Sec. V, we discussed how scattering to antitrapping states can be the limiting factor in the optical trapping lifetime. This conclusion is supported by a quantitative analysis of other sources of heating, which include collisions with background gas particles and recoil heating from photon scattering.

Since the ion trap chamber is not a perfect vacuum, ions can collide with background gas particles (mostly hydrogen molecules). Using the Langevin collision model, we find that the Langevin collision rate of a single ion with hydrogen molecules is only 1.3 per hour for a pressure of 10^{-11} mbar at room temperature. Although a Langevin collision event can provide enough energy for the ion to escape the trap, the collision rate is negligibly small compared to the typical optical trapping lifetime. There are non-Langevin collisions, with the impact parameter being larger than a critical value, such that the gas particles are not "captured" by the ion. Significantly smaller energies are exchanged between the two particles after the collision. The non-Langevin collision rate is also relatively small compared to the expected optical trapping lifetime. Our calculations show that the heating rate caused by non-Langevin collisions with hydrogen molecules is less than

0.1 mK/s for each ion under 10^{-11} mbar pressure and 300 K temperature.

Recoil heating caused by the photon scattering from the optical cavity trapping beam is even less impactful. For a $^{171}Yb^{+}$ ion interacting with a $\lambda = 1064$ nm laser, the recoil energy is $E_{\mathrm{rec}} \approx 5 \times 10^{-5}$ mK $\times k_B$ per ion per scattering event. Since 1064 nm is a far-detuned laser for a $^{171}Yb^{+}$ ion such that the off-resonant scattering rate is suppressed (see Table I), this recoil heating rate should have a negligible impact on the optical trapping lifetime.

[1] H. Diep and W. Scientific, *Frustrated Spin Systems* (World Scientific, Singapore, 2013).
[2] R. Moessner and A. P. Ramirez, Phys. Today **59**(2), 24 (2006).
[3] X. G. Wen, Phys. Rev. B **44**, 2664 (1991).
[4] L. Savary and L. Balents, Rep. Prog. Phys. **80**, 016502 (2017).
[5] C. Monroe, W. C. Campbell, L.-M. Duan, Z.-X. Gong, A. V. Gorshkov, P. W. Hess, R. Islam, K. Kim, N. M. Linke, G. Pagano, P. Richerme, C. Senko, and N. Y. Yao, Rev. Mod. Phys. **93**, 025001 (2021).
[6] R. Blatt and C. F. Roos, Nat. Phys. **8**, 277 (2012).
[7] S. Seidelin, J. Chiaverini, R. Reichle, J. J. Bollinger, D. Leibfried, J. Britton, J. H. Wesenberg, R. B. Blakestad, R. J. Epstein, D. B. Hume, W. M. Itano, J. D. Jost, C. Langer, R. Ozeri, N. Shiga, and D. J. Wineland, Phys. Rev. Lett. **96**, 253003 (2006).
[8] R. Schmied, J. H. Wesenberg, and D. Leibfried, Phys. Rev. Lett. **102**, 233002 (2009).
[9] T. Schaetz, A. Friedenauer, H. Schmitz, L. Petersen, and S. Kahra, J. Mod. Opt. **54**, 2317 (2007).
[10] B. Yoshimura, M. Stork, D. Dadic, W. C. Campbell, and J. K. Freericks, EPJ Quantum Technol. **2**, 2 (2015).
[11] R. Nath, M. Dalmonte, A. W. Glaetzle, P. Zoller, F. Schmidt-Kaler, and R. Gerritsma, New J. Phys. **17**, 065018 (2015).
[12] P. Richerme, Phys. Rev. A **94**, 032320 (2016).
[13] J. W. Britton, B. C. Sawyer, A. C. Keith, C.-C. J. Wang, J. K. Freericks, H. Uys, M. J. Biercuk, and J. J. Bollinger, Nature (London) **484**, 489 (2012).
[14] R. C. Sterling, H. Rattanasonti, S. Weidt, K. Lake, P. Srinivasan, S. C. Webster, M. Kraft, and W. K. Hensinger, Nat. Commun. **5**, 3637 (2014).
[15] C. D. Bruzewicz, R. McConnell, J. Chiaverini, and J. M. Sage, Nat. Commun. **7**, 13005 (2016).
[16] M. Gärttner, J. G. Bohnet, A. Safavi-Naini, M. L. Wall, J. J. Bollinger, and A. M. Rey, Nat. Phys. **13**, 781 (2017).
[17] F. Hakelberg, P. Kiefer, M. Wittemer, U. Warring, and T. Schaetz, Phys. Rev. Lett. **123**, 100504 (2019).
[18] Y. Wang, M. Qiao, Z. Cai, K. Zhang, N. Jin, P. Wang, W. Chen, C. Luan, B. Du, H. Wang, Y. Song, D. Yum, and K. Kim, Adv. Quantum Technol. **3**, 2000068 (2020).
[19] P. C. Holz, S. Auchter, G. Stocker, M. Valentini, K. Lakhmanskiy, C. Rössler, P. Stampfer, S. Sgouridis, E. Aschauer, Y. Colombe, and R. Blatt, Adv. Quantum Technol. **3**, 2000031 (2020).
[20] M. D'Onofrio, Y. Xie, A. J. Rasmusson, E. Wolanski, J. Cui, and P. Richerme, Phys. Rev. Lett. **127**, 020503 (2021).
[21] Y. Xie, J. Cui, M. D'Onofrio, A. J. Rasmusson, S. W. Howell, and P. Richerme, Quantum Sci. Technol. **6**, 044009 (2021).
[22] D. Kiesenhofer, H. Hainzer, A. Zhdanov, P. C. Holz, M. Bock, T. Ollikainen, and C. F. Roos, PRX Quantum **4**, 020317 (2023).
[23] D. Porras and J. I. Cirac, Phys. Rev. Lett. **92**, 207901 (2004).
[24] A. Friedenauer, H. Schmitz, J. T. Glueckert, D. Porras, and T. Schaetz, Nat. Phys. **4**, 757 (2008).
[25] M. Qiao, Z. Cai, Y. Wang, B. Du, N. Jin, W. Chen, P. Wang, C. Luan, E. Gao, X. Sun, H. Tian, J. Zhang, and K. Kim, Nat. Phys. (2024), doi:10.1038/s41567-023-02378-9.
[26] Y. H. Teoh, M. Drygala, R. G. Melko, and R. Islam, Quantum Sci. Technol. **5**, 024001 (2020).
[27] S. Korenblit, D. Kafri, W. C. Campbell, R. Islam, E. E. Edwards, Z.-X. Gong, G.-D. Lin, L.-M. Duan, J. Kim, K. Kim, and C. Monroe, New J. Phys. **14**, 095024 (2012).
[28] F. Rajabi, S. Motlakunta, C.-Y. Shih, N. Kotibhaskar, Q. Quraishi, A. Ajoy, and R. Islam, npj Quantum Inf. **5**, 32 (2019).
[29] C. Schneider, M. Enderlein, T. Huber, S. Dürr, and T. Schaetz, Phys. Rev. A **85**, 013422 (2012).
[30] J. Schmidt, A. Lambrecht, P. Weckesser, M. Debatin, L. Karpa, and T. Schaetz, Phys. Rev. X **8**, 021028 (2018).
[31] M. Enderlein, T. Huber, C. Schneider, and T. Schaetz, Phys. Rev. Lett. **109**, 233004 (2012).
[32] D. Hoenig, F. Thielemann, L. Karpa, T. Walker, A. Mohammadi, and T. Schaetz, arXiv:2306.12518.
[33] A. Lambrecht, J. Schmidt, P. Weckesser, M. Debatin, L. Karpa, and T. Schaetz, Nat. Photonics **11**, 704 (2017).
[34] O. Wipfli, H. F. Passagem, C. Fischer, M. Grau, and J. P. Home, Rev. Sci. Instrum. **94**, 083204 (2023).
[35] R. B. Linnet, I. D. Leroux, M. Marciante, A. Dantan, and M. Drewsen, Phys. Rev. Lett. **109**, 233005 (2012).
[36] D. Gangloff, A. Bylinskii, I. Counts, W. Jhe, and V. Vuletić, Nat. Phys. **11**, 915 (2015).
[37] G. R. Guthöhrlein, M. Keller, K. Hayasaka, W. Lange, and H. Walther, Nature (London) **414**, 49 (2001).
[38] H. Takahashi, E. Kassa, C. Christoforou, and M. Keller, Phys. Rev. Lett. **124**, 013602 (2020).
[39] A. Ransford, Ph.D. thesis, University of California, Los Angeles, 2020.
[40] M. Block, A. Drakoudis, H. Leuthner, P. Seibert, G. Werth, M. Block, A. Drakoudis, H. Leuthner, and P. Seibert, J. Phys. B **33**, L375 (2000).
[41] K. Mølmer and A. Sørensen, Phys. Rev. Lett. **82**, 1835 (1999).
[42] A. Sørensen and K. Mølmer, Phys. Rev. Lett. **82**, 1971 (1999).
[43] D. H. E. Dubin, Phys. Rev. Lett. **71**, 2753 (1993).
[44] J. P. Schiffer, Phys. Rev. Lett. **70**, 818 (1993).
[45] M. Schacht, J. R. Danielson, S. Rahaman, J. R. Torgerson, J. Zhang, and M. M. Schauer, J. Phys. B **48**, 065003 (2015).
[46] S. Olmschenk, K. C. Younge, D. L. Moehring, D. N. Matsukevich, P. Maunz, and C. Monroe, Phys. Rev. A **76**, 052314 (2007).
[47] Y. H. Teoh, M. Sajjan, Z. Sun, F. Rajabi, and R. Islam, Phys. Rev. A **104**, 022420 (2021).

[48] K. Kim, M.-S. Chang, R. Islam, S. Korenblit, L.-M. Duan, and C. Monroe, Phys. Rev. Lett. **103**, 120502 (2009).

[49] N. Kotibhaskar, C.-Y. Shih, S. Motlakunta, A. Vogliano, L. Hahn, Y.-T. Chen, and R. Islam, arXiv:2307.04922.

[50] N. Davidson, H. J. Lee, C. S. Adams, M. Kasevich, and S. Chu, Phys. Rev. Lett. **74**, 1311 (1995).

[51] T. Müller-Seydlitz, M. Hartl, B. Brezger, H. Hänsel, C. Keller, A. Schnetz, R. J. C. Spreeuw, T. Pfau, and J. Mlynek, Phys. Rev. Lett. **78**, 1038 (1997).

[52] F. Gerbier and Y. Castin, Phys. Rev. A **82**, 013615 (2010).

[53] S. Motlakunta, N. Kotibhaskar, C.-Y. Shih, A. Vogliano, D. Mclaren, L. Hahn, J. Zhu, R. Hablützel, and R. Islam, arXiv:2306.03075.